ARL-TR-10370 ● JUNE 2026

A Process Model for Age Hardening of Crossover Alloy AA5180

by Taylor W. Cain

NOTICES

Disclaimers

The findings in this report are not to be construed as an official Department of the Army position unless so designated by other authorized documents.

Citation of manufacturer's or trade names does not constitute an official endorsement or approval of the use thereof.

Destroy this report when it is no longer needed. Do not return it to the originator.

ARL-TR-10370 ● JUNE 2026

A Process Model for Age Hardening of Crossover Alloy AA5180

Taylor W. Cain
DEVCOM Army Research Laboratory

REPORT DOCUMENTATION PAGE

1. REPORT DATE	2. REPORT TYPE	3. DATES COVERED	
		START DATE	END DATE
June 2026	Technical Report	11/1/2022	3/30/2026

4. TITLE AND SUBTITLE
A Process Model for Age Hardening of Crossover Alloy AA5180

5a. CONTRACT NUMBER	5b. GRANT NUMBER	5c. PROGRAM ELEMENT NUMBER
5d. PROJECT NUMBER	**5e. TASK NUMBER**	**5f. WORK UNIT NUMBER**

6. AUTHOR(S)
Taylor W. Cain

7. PERFORMING ORGANIZATION NAME(S) AND ADDRESS(ES)
DEVCOM Army Research Laboratory
ATTN: FCDD-RLA-MF
Aberdeen Proving Ground, MD 21005

8. PERFORMING ORGANIZATION REPORT NUMBER
ARL-TR-10370

9. SPONSORING/MONITORING AGENCY NAME(S) AND ADDRESS(ES)	10. SPONSOR/MONITOR'S ACRONYM(S)	11. SPONSOR/MONITOR'S REPORT NUMBER(S)

12. DISTRIBUTION/AVAILABILITY STATEMENT
DISTRIBUTION STATEMENT A. Approved for public release: distribution unlimited.

13. SUPPLEMENTARY NOTES
ORCID: Taylor W. Cain, 0000-0002-6621-914X

14. ABSTRACT
A process model describing the change in hardness with time as a function of isothermal aging temperature was performed on the crossover 5XXX series aluminum alloy 5180 for the first time. The process model suggested the presence of two dominant strengthening precipitates, with a transition temperature near 131 °C defining a low- and high-temperature precipitate. The process model showed good agreement with the experimental data, and the final derived parameters remained physically justified. The aging kinetics at temperatures below 100 °C were predicted to be very slow, exemplifying the superior resistance to microstructural change compared with conventional 5XXX series alloys.

15. SUBJECT TERMS
Sciences of Extreme Materials, crossover alloy, 5xxx series alloy, precipitation hardenable, process model

16. SECURITY CLASSIFICATION OF:			17. LIMITATION OF ABSTRACT	18. NUMBER OF PAGES
a. REPORT	b. ABSTRACT	C. THIS PAGE		
UNCLASSIFIED	UNCLASSIFIED	UNCLASSIFIED	UU	43

19a. NAME OF RESPONSIBLE PERSON	19b. PHONE NUMBER *(Include area code)*
Taylor W. Cain	(520) 691-5035

STANDARD FORM 298 (REV. 5/2020)
Prescribed by ANSI Std. Z39.18

Contents

List of Figures

List of Tables

1. Introduction

The development of 5XXX series Al–Mg-based alloys with nontraditionally high concentrations of Zn has provided an exciting composition space that has been largely unexplored in open literature. However, more than 60 peer-reviewed articles have been published exploring this composition space for wrought alloy products since a U.S. patent was issued to ALCOA Inc., in 2016.[1,2] The alloys, recently dubbed "crossover alloys," are able to be strengthened via precipitation hardening without the use of expensive exotic elements such as Sc, Y, and Er and can be easily produced within current recycling streams used by the aluminum industrial base.[2] These alloys can be strengthened by additions of Zn (typically between 2.0 and 5.0 wt%) with up to 1 wt% addition of Cu that shifts the equilibrium phase diagram from an α + β-Al_3Mg_2 phase field to an α + τ-$Mg_{32}(Al,Zn,Cu)_{49}$ phase field. Formation of the equilibrium τ-phase generally follows a precipitation sequence from a supersaturated solid solution to retain the α phase, which precipitates one or multiple metastable phases before reaching the equilibrium τ-phase whereby the metastable variants of τ-phase provide the precipitation-hardening effect.[3,4] In contrast, traditional 5XXX series wrought products rely on solid-solution strengthening and strain hardening as the primary strengthening mechanisms because Al–Mg-based precipitates do not provide precipitation hardening. However, the integration of precipitation hardening allows significantly higher strengths while maintaining the low-density benefits inherent to magnesium. To achieve optimal performance in metrics such as yield strength, fracture toughness, and corrosion resistance, a precise understanding of thermomechanical-processing routes and the corresponding microstructure underpinning material performance is required. To this end, process models serve as critical tools, establishing mathematical relationships between variables such as chemical composition and heat treatment parameters to determine material properties based on fundamental physical principles.

A first-of-its-kind process model for age hardening of aluminum alloys was established by Shercliff and Ashby in 1990.[5,6] Their process model was successfully applied to 2XXX and 6XXX series aluminum alloys for isothermal heat treatments[5] and non-isothermal heat treatments[6] applied in heat-affected zones during welding. This process model has primary advantages, including not needing knowledge of the exact nature of precipitate composition, size, distribution, and identity that usually requires time-consuming preparation and analysis via transmission electron microscopy (TEM) or small-angle X-ray scattering. The process model can be computed as often as needed based on modified experimental heat treatment data and temperatures. Later process models, such as those proposed

by Deschamps and Brechet,[7] Deschamps et al.,[8] Zhu et al.,[9] Zhu and Starke,[10] Myhr et al.,[11] and Robson,[12] utilized more complex models that incorporated the nature of precipitates to successfully predict strength.

This investigation evaluates the efficacy of the Shercliff and Ashby[5,6] process model to predict the isothermal-hardening behavior of registered crossover alloy AA5180 (henceforth noted as 5180). This model was selected for its simplicity because it only needs experimental age-hardening curves to calibrate the model in lieu of extensive TEM analysis. Eight experimental age-hardening curves were generated at temperatures ranging from 105 to 225 °C for durations up to 4,344 h to build a first-of-its-kind database for 5180 to calibrate the process model.

2. Methods and Theory

2.1 Experimental Methods

A high Cu variant of 5180 was used during this study, and the actual composition is found in Table 1. Samples approximately 1/4 × 1/4 × 1 inch were sectioned from a 1-inch-thick plate of 5180 in the T10 temper for heat treatment studies. The samples were exposed to solution treatment at 485 °C for 1 h to remove any cold work in a muffle furnace and then water quenched at room temperature. The water-quenched samples were immediately artificially aged in either an oil bath or laboratory convection oven depending on the temperature specified in Table 2 and subsequently water quenched after completing the designated aging time. The temperature in the oil bath was monitored using an independent K-type thermocouple, whereas temperature in the convection ovens was monitored using a 5180 sample with a K-type thermocouple inserted into it.

Table 1. The composition of 5180 as measured by inductively coupled plasma-optical emission spectrometry in wt%.

Alloy	Al	Mg	Zn	Cu	Mn	Zr	Ti	Fe	Cr	Ni	Si	Sc
Nominal	Bal	3.5–4.5	1.7–2.8	0.1	0.2–0.7	0.08–0.25	0.06–0.2	. . .[a]	. . .	. . .	. . .[a]	. . .
Actual	Bal	3.953	2.286	0.226	0.191	0.148	0.096	0.041	0.002	0.006	0.078	0.037

[a] Indicates 0.35 wt% Si + Fe.

Table 2. The type of equipment used to heat treat samples at each of the specified temperatures.

Temperature (°C)	Equipment
105	Oil bath
115	Convection oven
125	Convection oven
140	Convection oven
155	Convection oven
170	Convection oven
200	Convection oven
225	Convection oven

Rockwell B hardness (HRB) was measured on each sample using a Wilson Instruments Rockwell Hardness Tester by taking the mean of five measurements. Before hardness measurements, samples were ground to a Coated Abrasive Manufacturers Institute (CAMI) 600-grit finish using silicon carbide (SiC) papers to remove any surface films from heat treatment and to ensure samples were flat and parallel. The HRB data was transformed to Vickers hardness (VH) units using ASTM E140-12B(2019)e1.[13] An internal calibration curve was generated on various crossover alloys for similitude to verify the validity of ASTM E140-12B(2019)e1 over the range of Rockwell hardness values measured in this study.

Samples for Vicker hardness testing were prepared by grinding samples to a CAMI 1200-grit finish using SiC grinding papers and polished successively with 1- and 0.25-µm water-based, diamond-polishing slurries, rinsed with deionized water, and dried under compressed laboratory air. A minimum of 10 Vickers hardness measurements were performed on a Mitutoyo HM-200 Vickers hardness tester was used with a 1-kgf load with a 5-s load time, 10-s dwell time, and 5-s unload time.

After completion of Vickers hardness measurements, five HRB measurements were taken on the same samples as described above. Conversion of hardness data from HRB to VH was necessary for the process model because the round ball used for HRB measurements produces a nonlinear gradient of hardness, whereas the Vickers hardness method produces a linear hardness gradient due to the geometry of the diamond indenter. The collected data showed excellent agreement within one standard deviation of the mean to ASTM E140-12B(2019)e1,[13] as shown in Figure 1.

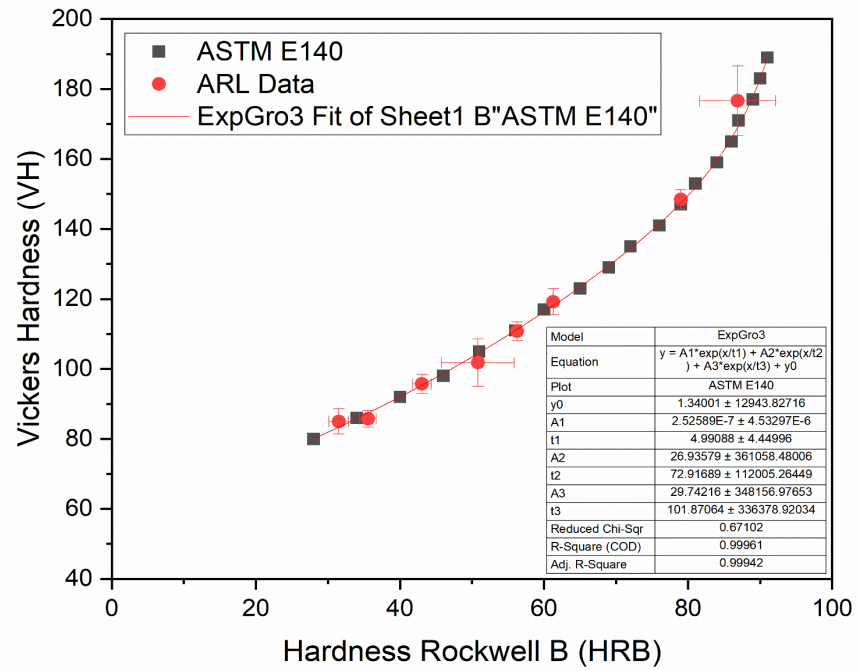

Figure 1. Plot of HRB vs. VH comparing data from ASTM E140-12B(2019)e1[13] to internally generated data on various crossover alloys.

Transformation of all HRB data measured in this study was transformed to VH via the following transfer function of ASTM E140 in Equation 1, where *VH* is the Vickers hardness number and *HRB* is the measured Rockwell B hardness.

$$VH = 2.526 \times 10^{-7}\left(\frac{HRB}{4.991}\right) + 26.936\left(\frac{HRB}{72.917}\right) + 29.742\left(\frac{HRB}{101.871}\right) + 1.340 \quad (1)$$

2.2 The Process Model

2.2.1 Components of the Physical Model

Complete details for the derivations and theoretical assumptions of the process model can be found in the manuscript by Shercliff and Ashby,[5] but the relevant assumptions and equations needed to complete the process model are provided below. The primary expressions developed for the process model are based on the following:

- The contributions of solid solution to the strength as a function of precipitate volume fraction and solute concentration in the matrix.
- The dependence of equilibrium precipitate volume fraction as a function of temperature.
- Coarsening of precipitates by competitive growth.
- The contributions of shearable and non-shearable precipitates to the strength.

The total hardness (H_{tot}) due to precipitation hardening is composed of the intrinsic hardness (H_i), solid-solution hardness (ΔH_{ss}), and precipitate hardness (ΔH_{ppt}), where the intrinsic hardness includes the hardness of aluminum, contributions of stable phases, contributions of grain-size strengthening, and any other contribution which is assumed to be constant during aging:

$$H_{tot} = H_i + \Delta H_{SS} + \Delta H_{ppt} \tag{2}$$

The solid-solution hardening component can be written as Equation 3.

$$\Delta H_{SS} = \left[\Delta H_{ss0}^{3/2} + \left(\Delta H_{ssi}^{3/2} - \Delta H_{ss0}^{3/2}\right)\exp\left(-\frac{t}{t_1}\right)\right]^{2/3}, \tag{3}$$

where ΔH_{SS} is the final solid-solution strengthening contribution after the equilibrium volume fraction of precipitates has been reached, ΔH_{ssi} is the initial solid-solution strengthening hardening contribution after quenching, t is the aging time, and t_1 is a constant related to the time-to-peak hardness (t_p) and a constant k whose value lies between 0 and 1:

$$t_1 = kt_p \tag{4}$$

The value for ΔH_{ssi} is the difference between the as-quenched hardness (H_q) and the intrinsic hardness (H_i), where the intrinsic hardness is assumed to be 15 HV for aluminum, whereas the value for ΔH_{Ss0} is the difference between the overaged hardness ($\Delta H_{ss,oa}$) and the intrinsic hardness.

$$\Delta H_{ss0} = \Delta H_{ss,oa} - H_i \tag{5}$$

The overaged hardness is determined from known values of H_i and H_q following Equation 6:

$$\Delta H_{ss,oa} = H_i + \left(H_q - H_i\right)exp\left[\frac{-2Q_s}{3R}\left(\frac{1}{T} - \frac{1}{T_s}\right)\right], \tag{6}$$

where Q_s is the free energy of solution of the solute, R is the ideal gas constant, T is the aging temperature in units of K, and T_s is the metastable solvus temperature of the strengthening precipitate in units of K. Values for Q_s and T_s are derived from experimental data in the calibration procedure that is described in Section 2.2.2.

The contribution of age-hardenable precipitates to hardness is based on synergy between shearable and non-shearable precipitates whose contributions are related to the precipitate volume fraction and precipitate radius, which is assumed to be spherical. Shercliff and Ashby[5,6] gave the following contributions of precipitates to hardness (Equation 7):

$$\Delta H_{ppt} = \frac{2S(P^*)^{1/6}}{1+(P^*)^{1/2}}, \quad (7)$$

where S is the peak precipitate strength and $P^* = P/P_p$. The temperature corrected time (P) for a fixed volume fraction is given by

$$P = \frac{t}{T} exp\left(\frac{-Q_a}{RT}\right), \quad (8)$$

where Q_a is the activation energy for volume diffusion of atoms in the matrix, and P_p is the value of P at the peak in the aging curve. The precipitate strength (S_o) as a function of time and aging temperature is given by

$$(S_0)^2 = (S_0)^2_{max}\left[1 - exp\left(\frac{Q_s}{R}\right)\left(\frac{1}{T} - \frac{1}{T_s}\right)\right], \quad (9)$$

where $(S_o)_{max}$ is the strength parameter that is found after the calibration procedure.

2.2.2 The Calibration Procedure

Shercliff and Ashby[5] structured the above equations such that the unknown constants can be determined from aging curves after an iterative calibration process. The steps to calibration are as follows:

1) Choose values for the as-quenched hardness (H_q) and the intrinsic strength (H_i) and calculate a first estimate of $\Delta H_{ss,oa}$ halfway between the two values. A first estimate is needed because $\Delta H_{ss,oa}$ is dependent on the aging temperature and unknowns Q_s and T_s.
2) Determine the time-to-peak aging and the peak hardness for as many temperatures as possible.
3) Make a plot of $\ln(t_p/T)$ vs. $1000/T$ and measure the slope, Q_a/R, to determine Q_a where R = 8.314 J/mol-K.
4) Calculate P_p for each aging temperature and use the mean of P_p for the remaining calculations.
5) Evaluate ΔH_{ppt} for each temperature using the value determined for Q_a and calculate S_0 as the difference between the peak hardness and estimated $\Delta H_{ss,oa}$.
6) Plot $(S_0)^2$ vs. aging temperature (in units of K) and extrapolate the data curve to $(S_0)^2 = 0$ to give an estimate of T_s.
7) Estimate $(S_0)^2_{max}$ from the lower-temperature plateau and calculate Q_s at each temperature using Equation 9. Use the average value to compute the first estimate of Q_s.
8) Repeat steps 1–7 inserting values for $\Delta H_{ss,oa}$ using Equation 6 to provide a more accurate estimate of $\Delta H_{ss,oa}$ using k = 0.5 and continue until a

satisfactory fit between theory and data is reached. Final tuning of the process model can be performed by adjusting k.

After a satisfactory fit is made, the parameters can be further optimized by performing sensitivity analysis. The above process applies for a single strengthening precipitate; however, if multiple strengthening precipitates are involved, then a transition temperature needs to be determined from the data using the Arrhenius plot of peak corrected time and the plot of $(S_0)^2$ versus aging temperature. For example, data for a low-temperature and high-temperature regime have the same calibration procedure as that for data which falls above and below the transition temperature. This may cause difficulty in estimations of T_s and $(S_0)^2_{max}$, particularly in the low-temperature regime, where data may be sparse due to the long aging times needed to reach peak aging and lack of appearance of a clear plateau in the plot of $(S_0)^2$ versus aging temperature.

3. Results

3.1 Age-Hardening Results

The mean measured hardness as a function of aging time and temperature is shown in Figure 2, and the relevant peak hardness data needed for the process model is given in Table 3. Each of the hardness curves shows a defined peak, except for the aging temperature of 105 °C, which appears to increase hardness after 3,024 h of aging and 115 °C. This temperature appears to be nearing peak hardness after 4,344 h of aging. Based on the nature of the hardening curves, the peak hardness data for 105 °C will not be used in further calculations, but the peak hardness for 115 °C is assumed to be a valid peak hardness.

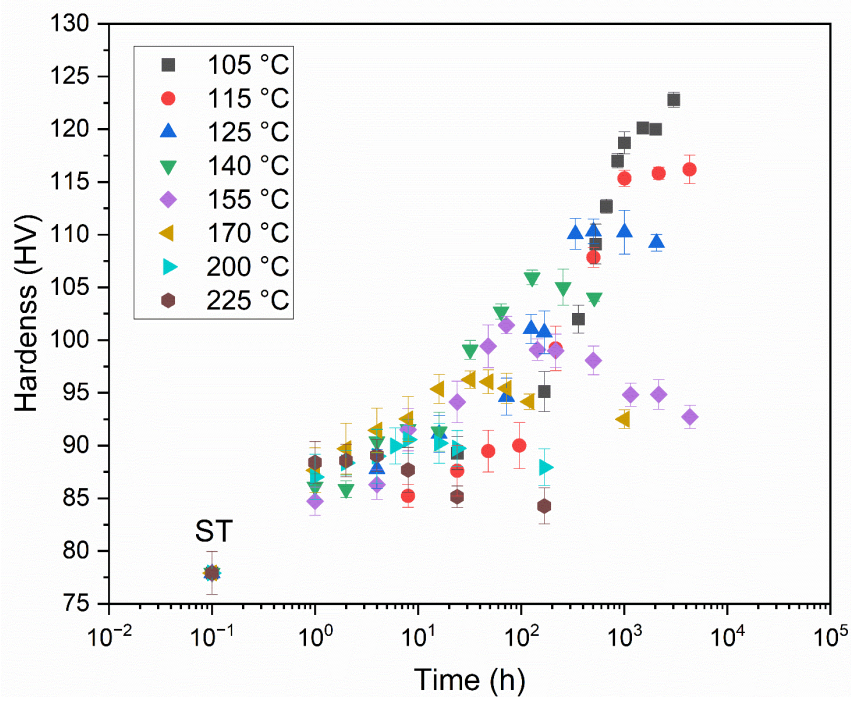

Figure 2. The mean hardness vs. time measured at different temperatures. Error bars are 1 standard deviation of the mean, and "ST" indicates the solution-treated hardness.

Table 3. The mean peak hardness measured and time to reach peak hardness (t_p).

Aging temperature (°C)	Peak hardness (HV)	Time-to-peak hardness (h)
105	122.8 ± 0.72	. . .
115	116.2 ± 1.34	4320
125	110.3 ± 1.16	504
140	105.9 ± 0.705	128
155	101.4 ± 0.83	72
170	96.2 ± 0.82	32
200	90.6 ± 1.3	8
225	89.1 ± 1.5	4

3.2 First Iteration of the Process Model

For the first iteration of the process model, $\Delta H_{ss,oa}$ was assumed to be 46.45 with an intrinsic strength of 15 HV and an as-quenched hardness of 77.9 HV. The Arrhenius plot of the time-to-peak hardness and aging temperature is shown in Figure 3. All linear-fitted data within OriginPro 2023b yielded a slope of approximately 11,650 K, providing 96,858 J/mol for Q_a, which was used to calculate the initial P_p. The average value for P_p was 1.46×10^{-9}, which was used in Equation 7 to compute the hardness contribution of precipitates.

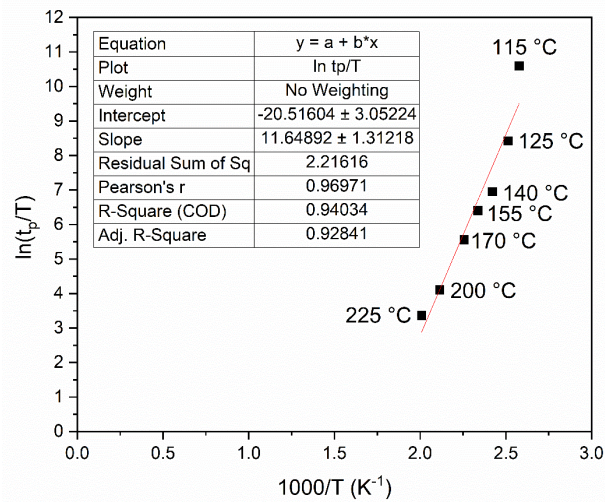

Figure 3. The Arrhenius plot of the peak-corrected time for calibration procedure with a single linear fit.

The first plot of $(S_0)^2$ versus aging temperature is shown in Figure 4 using the evaluated parameters in Table 4. Figure 4 revealed that $(S_0)^2$ increased to a vertical asymptote instead of a horizontal asymptote as the aging temperature approaches 0 K. This process indicates that additional low-temperature data are required to completely physically describe the precipitation-hardening response. Further inspection of the curve could also indicate a high- and low-temperature precipitate based on the curvature as temperature increases. However, this first iteration uses an approximation of the overaged hardness that is the same for all aging temperatures. This provides a first estimation, whereas the actual overaged strength at each temperature is dependent on the aging temperature, solvus enthalpy, and solvus temperature, as indicated in Equation 6.

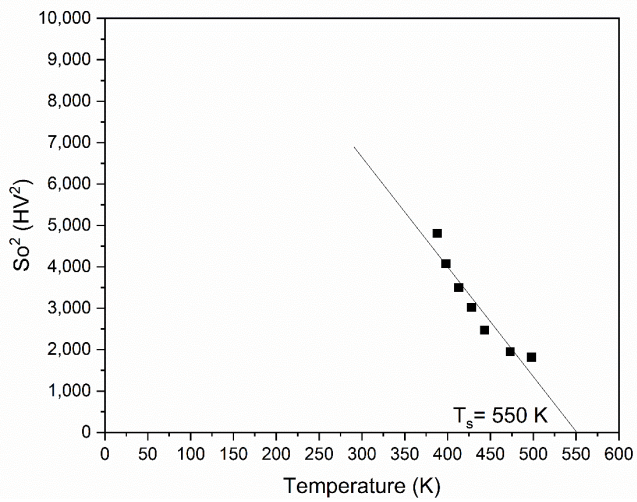

Figure 4. The first plot of $(S_0)^2$ vs. aging temperature.

Table 4. Data for the evaluated parameters at various aging temperatures.

T (°C)	T (K)	Pp (s/K)	S_0 (HV)	$(S_o)^2$ (HV^2)
115	388	3.66E-09	69.35	4809.4
125	398	8.84E-10	63.85	4076.8
140	431	5.87E-10	59.15	3498.7
155	428	9.14E-10	54.95	3019.5
170	473	9.86E-10	49.75	2475.1
200	498	1.22E-09	44.15	1949.2
225	498	2.00E-09	42.65	1819.0

The solvus temperature was approximated using a linear fit of all data in Figure 4 and determined at zero strength to be 550 K (277 °C). For the initial calculation of Q_s, $(S_0)^2_{max}$ was estimated to be 10,000 HV and values for each aging temperature are given in Table 5. The mean value for Q_s was then used to calculate $(S_0)^2$ versus temperature whose results show good agreement with the data given in Figure 5. In addition, a plot for the calculated values of $(S_0)^2$ versus aging temperature shows good agreement with the data shown in Figure 5.

Table 5. The evaluated values of Q_s at each temperature.

	115 °C	125 °C	140 °C	155 °C	170 °C	200 °C	225 °C	Mean
Q_s (j/mol)	7,182	6,271	5,936	5,767	5,384	6,090	8,792	6,489

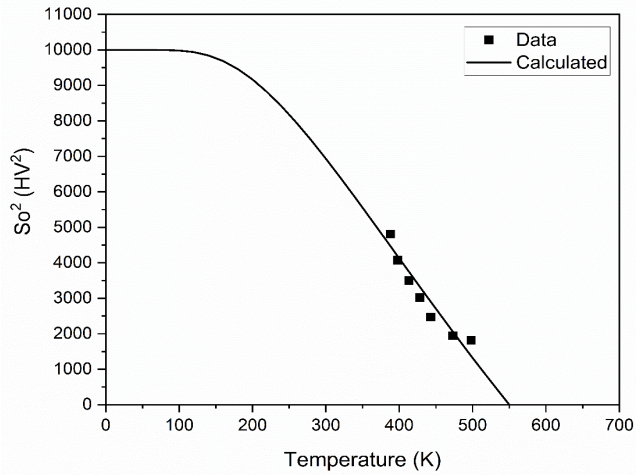

Figure 5. The plot of $(S_0)^2$ vs. aging temperature with the first calculated values of $(S_0)^2$.

The first iteration of hardness versus aging time for the process model (shown in Figure 6) reveals that further tuning of the model is needed. The model has captured the general shape of aging hardening at each temperature, but notable differences are present for the peak hardness, time-to-peak hardness, as well as poor matching of overaged data. Nonetheless, this first approximation shows promise for fitting the system with additional tuning.

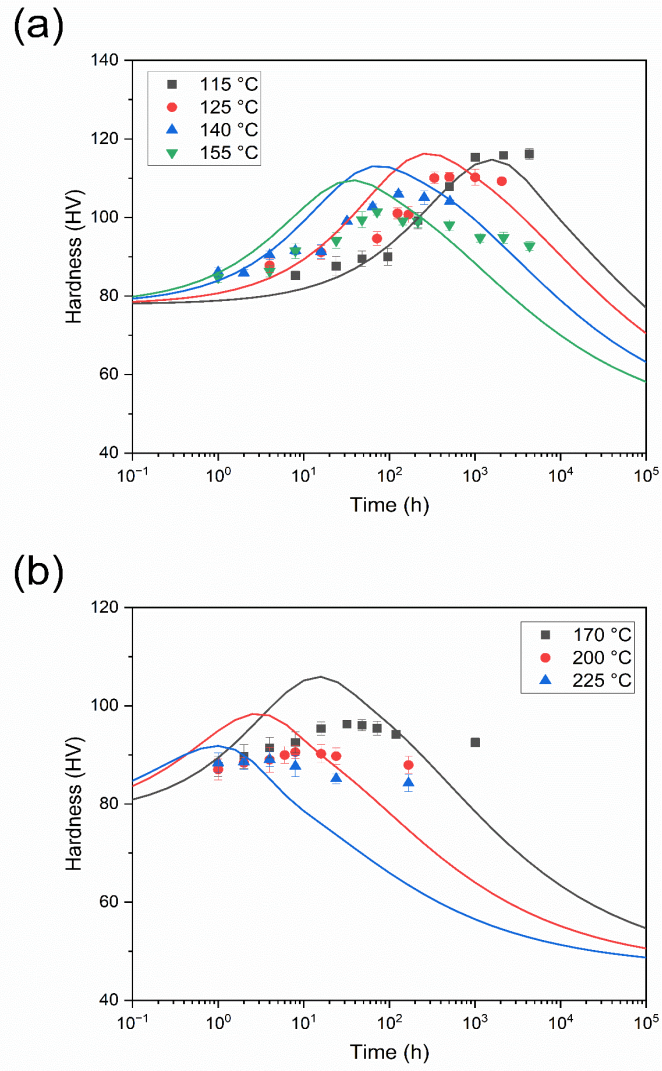

Figure 6. The first iteration of the predicted hardness based on the process model compared with the measured data: (a) shows lower temperatures and (b) shows higher temperatures. The solid-colored lines indicate the process model prediction for each temperature.

3.3 Continued Iterations for One Strengthening Precipitate

Several iterations of the process model were completed utilizing Equation 6 for the overaged strength: the final optimized parameters were determined in Microsoft Excel using the solver function. To complete this, the squared error (SE) was calculated for each predicted data point compared with the measured experimental data following

$$SE = \left(H_{meas} - H_{pred}\right)^2, \tag{10}$$

where the SE is determined by the measured hardness (H_{meas}) and the predicted hardness from the process model (H_{pred}). The sum of the SE was used as the

minimization criteria using the SE for each data point with equal weight. The generalized reduced gradient (GRG) nonlinear solving method was utilized with Q_a, T_s, $(S_0)^2_{max}$, and Q_s as variables to provide final fitting. The final optimized parameters lowered the sum SE from 435% to 166%, which indicated an improvement but far from an excellent fit. The corresponding fit of hardness is shown in Figure 7, and the accepted values for each parameter are given in Table 6. The model provided a close fit to the data for 140 and 225 °C while performing an adequately fitting time-to-peak hardness at each temperature. However, the model continued to poorly fit the low-temperature data, indicating that a model utilizing two strengthening precipitates may better capture the age-hardening response.

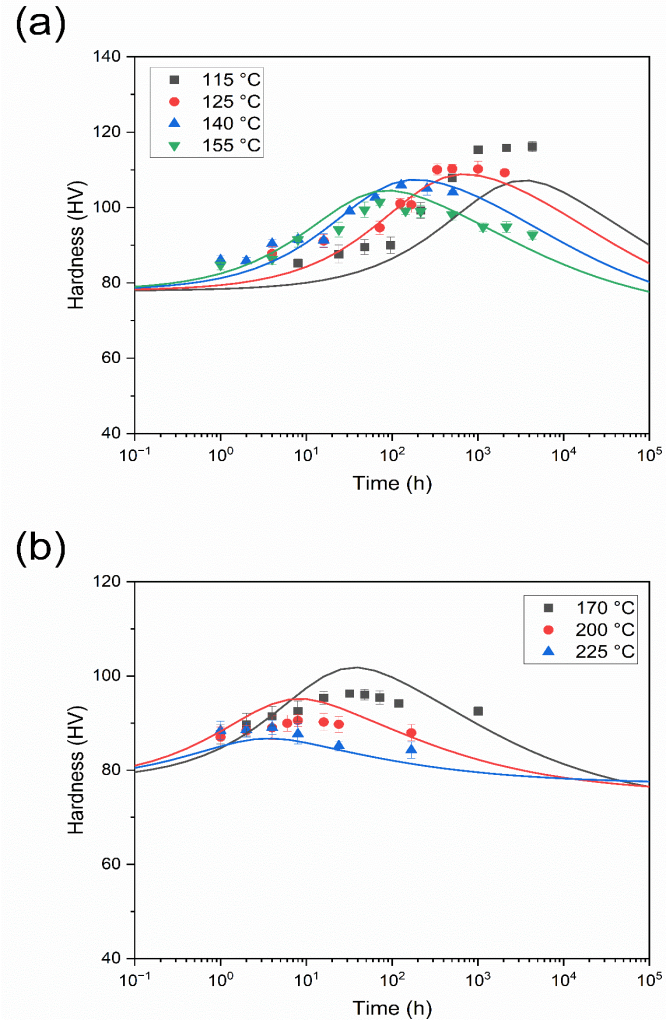

Figure 7. The final optimized iteration of the predicted hardness based on the process model compared with the measured data: (a) shows lower temperatures and (b) shows higher temperatures. The solid-colored lines indicate the process model prediction for each temperature.

Table 6. The accepted values for the process model after optimization.

Parameter	Accepted value
H_i	15
H_q	77.9
Q_a *(J/mol)*	119,828
T_s *(°C)*	235
$(S_0)^2_{max}$ *(HV²)*	6,566
Q_s *(J/mol)*	4,331
P_p *(s/k)*	2.75e-12
K	0.5

3.4 Process Model for Two Strengthening Precipitates

A new fitting of the peak-corrected time plot required selecting a transition temperature between a low-temperature and high-temperature precipitate that is assumed to dominate the hardening response. This temperature was approximately 140 °C, which was chosen for initial fitting of the activation energy based on Figure 3. Thus, determination of Q_a was performed with the low-temperature regime assessed on data ≤140 °C, whereas the high-temperature regime was assessed on data ≥140 °C. The data at 140 °C was considered part of the high-temperature regime for further fitting of the process model. Linear-fitted data are shown in Figure 8, where Q_a was determined to be 190,348 and 75,304 J/mol for the low-temperature and high-temperature regimes based on the evaluated slope.

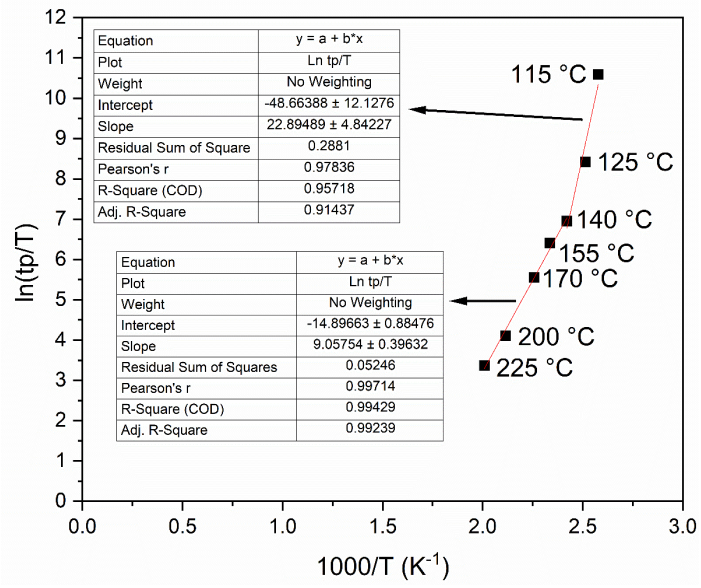

Figure 8. The Arrhenius plot of the peak-corrected time for the calibration procedure with two fitting regimes.

Estimation of T_s for each regime is shown in Figure 9 via linear extrapolation, where T_s was 457 and 577 K for the for the low- and high-temperature regime, respectively. Values for $(S_0)^2_{max}$ of each regime were assumed be 10,000 VH^2 for the low-temperature regime and 7,000 VH^2 for the high-temperature regime in the first approximation. This enabled calculation of Q_s at each temperature, as shown in Table 7. The mean Q_s was then calculated to generate initial hardness curves for each aging temperature.

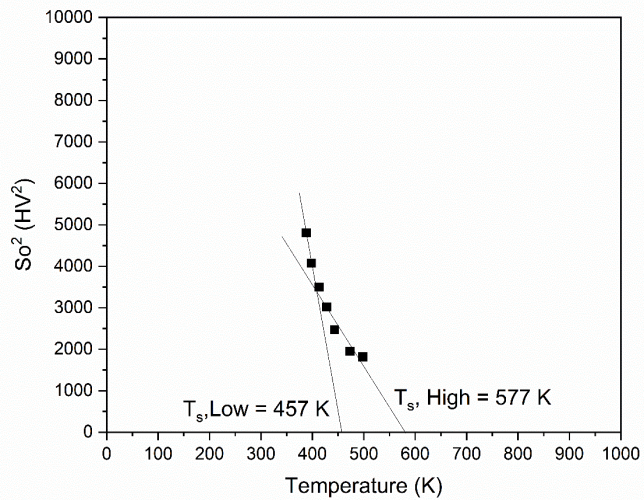

Figure 9. The first plot of $(S_0)^2$ vs. aging temperature showing linear extrapolation of the high- and low-temperature regimes to determine first estimation of T_s.

Table 7. Data for the initial evaluated parameters at various aging temperatures.

Regime	T (°C)	T (K)	Pp (s/K)	S_0 (HV)	$(S_o)^2$ (HV^2)	Q_s (J/mol)
Low temperature	115	388	9.47E-22	69.35	4809	16,026
	125	398	4.74E-22	63.85	40767	15,809
High temperature	140	431	3.13E-07	59.15	3498	8,369
	155	428	3.90E-07	54.95	3019	7,779
	170	473	3.43E-07	49.75	2475	6,920
	200	498	2.94E-07	44.15	1949	7,121
	225	498	3.65E-07	42.65	1819	9,100

The plot of the calculated $(S_0)^2_{max}$ versus aging temperature is shown in Figure 10 for the first estimation of the process model. The corresponding fit of the hardness versus aging time data is shown in Figure 11, which shows that further tuning is needed after the overaged hardness (described by Equation 6) is used in the process model.

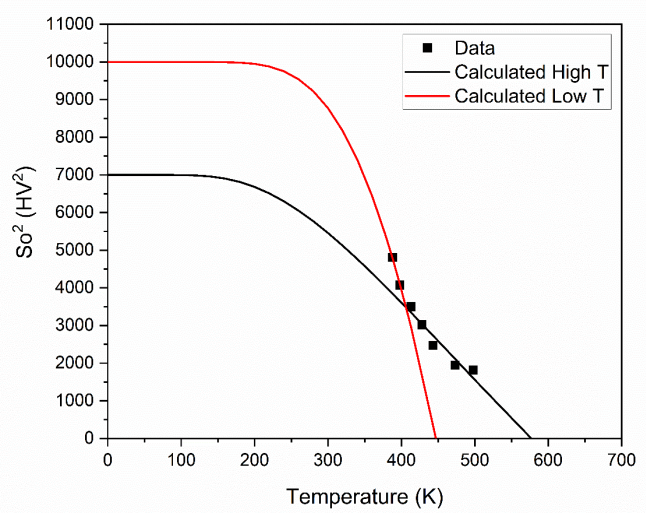

Figure 10. The plot of $(S_0)^2$ vs. aging temperature with the first calculated values of $(S_0)^2$ using a low-temperature (red line) and high-temperature regime (black line).

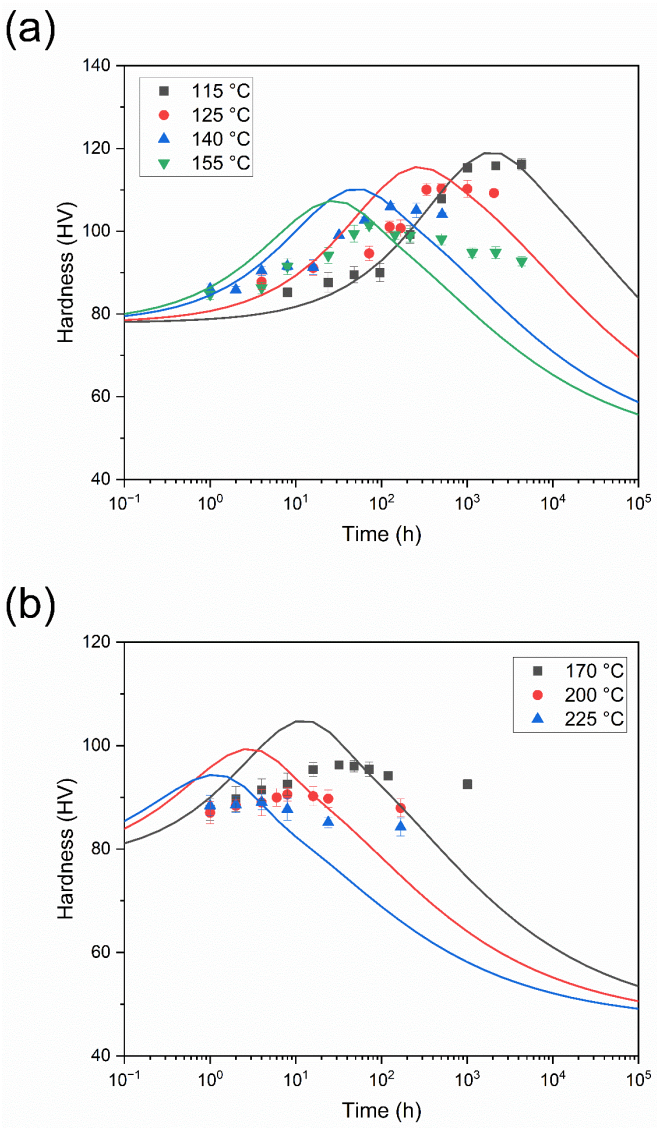

Figure 11. The first iteration of the predicted hardness based on two strengthening precipitates where (a) shows lower temperatures and (b) shows higher temperatures. The solid-colored lines indicate the process model prediction for each temperature.

The final plot of hardness versus aging time for the optimized process model is shown in Figure 12, and the final accepted values for the derived parameters are given in Tables 8 and 9. Inspection of the predicted hardness in Figure 12 shows good agreement with the data, but it is not a perfect fit. This result is also shown in Figure 13 with the plot of $(S_0)^2$ versus aging temperature. Individual plots of the predicted hardness versus measured hardness at each temperature are shown Figure 14, which further reinforces adequate fitting of the data.

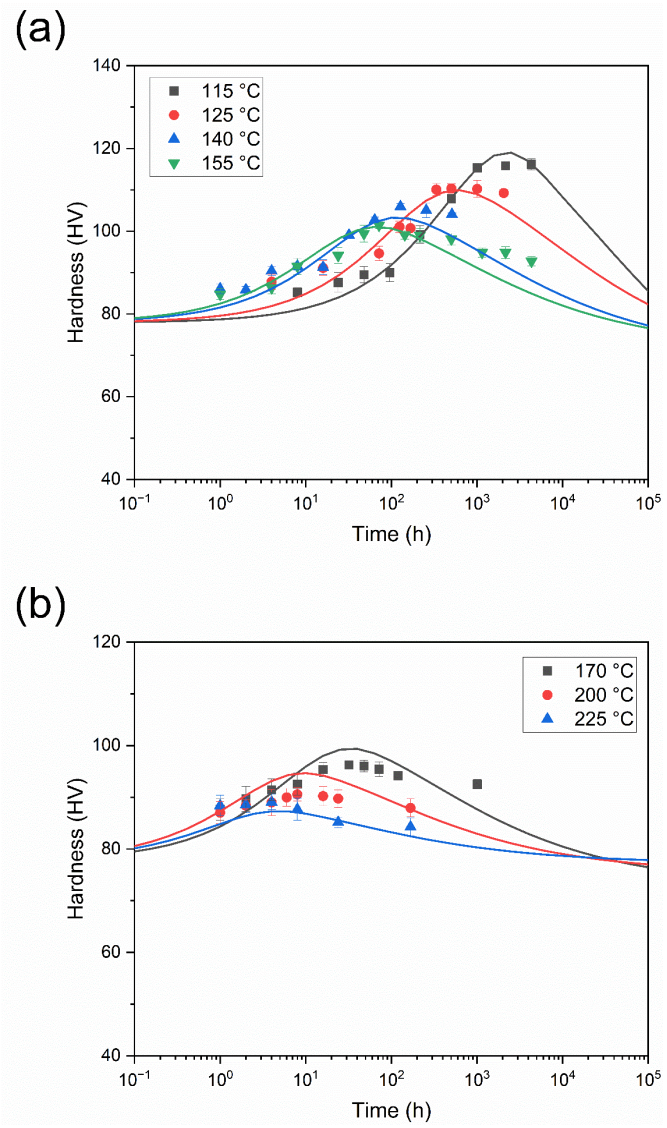

Figure 12. (a,b) The optimized fit of hardness vs. aging time for the process model incorporating two strengthening precipitates.

Table 8. Final data for the evaluated parameters at various aging temperatures for the process model with two strengthening precipitates.

T (°C)	T (K)	Pp (s/K)	S_0 (HV)	$(S_o)^2$ (HV^2)
115	388	2.61E-22	66.43	4,413
125	398	1.35E-22	43.73	1,913
140	413	3.42E-07	35.62	1,269
155	428	4.25E-07	30.02	901
170	443	3.73E-07	23.49	552
200	473	3.18E-07	15.39	237
225	498	3.93E-07	11.98	143

Table 9. Final accepted values for various constants in the process model with two strengthening precipitates.

Parameter	Accepted value
H_i	15 VH
H_q	77.9 VH
Q_a low temperature	194,500 J/mol
Q_a high temperature	75,000 J/mol
T_s low temperature	130 °C
T_s high temperature	236 °C
Q_s low temperature	78,141 J/mol
Q_s high temperature	3,685 J/mol
$(S_0)^2_{max}$ low temperature	7,475 HV^2
$(S_0)^2_{max}$ high temperature	6,411 HV^2
P_p low temperature	1.98×10^{-22}
P_p high temperature	3.70×10^{-7}
k low temperature	0.62
k high temperature	0.50

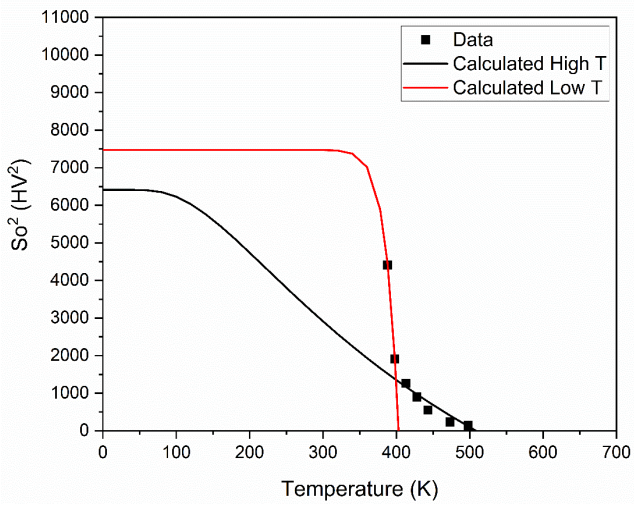

Figure 13. The plot of $(S_0)^2$ vs. aging temperature with the first calculated values of $(S_0)^2$ using a low-temperature (red line) and high-temperature regime (black line) for the process model with two strengthening precipitates.

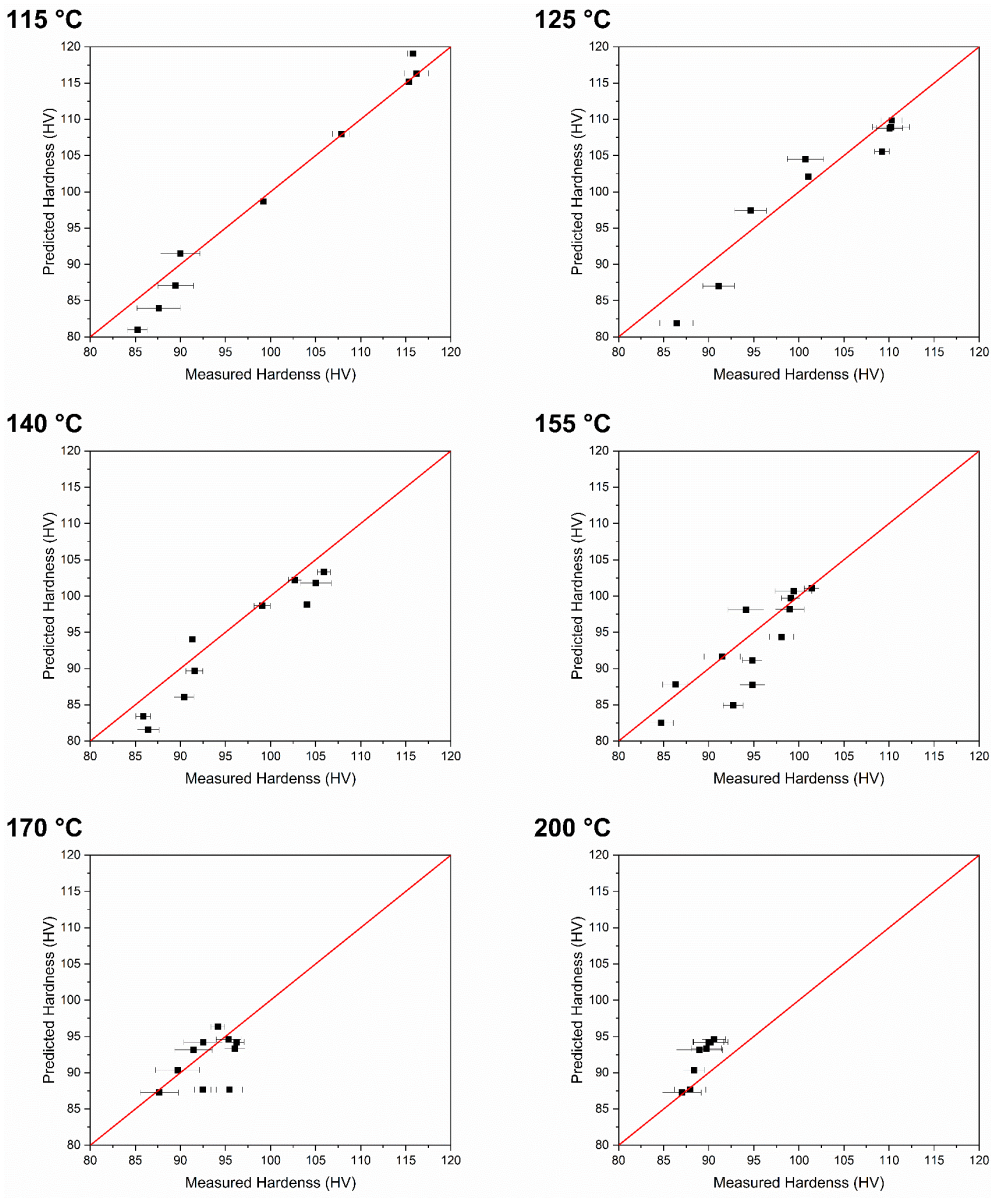

Figure 14. Plots of the predicted hardness vs. measured hardness for each aging temperature. The red line is a slope of 1.

3.5 Further Tuning of the Process Model with Two Strengthening Precipitates

The low-temperature regime was further tuned by using the collected hardness data at 105 °C. This was completed by allowing the solver function to calculate the time-to-peak hardness and peak hardness. The accepted value for the time-to-peak hardness was calculated to be 6,177 h with a peak hardness of 122 HV. The accepted values for the low-temperature regime after final iteration are given in Tables 10 and 11. Plots of the final calculated hardness versus time for the low-

temperature regime are shown in Figure 15, and the fit of $(S_0)^2$ versus aging temperature in Figure 16 shows excellent agreement between the experimental data and the calculated process model.

Table 10. Final data for the evaluated parameters in the low-temperature regime including data for 105 °C.

T (°C)	*T* (K)	*Pp* (s/K)	S_0 (HV)	$(S_o)^2$ (HV^2)
105	378	4.23E-17	77.28	5,972
115	388	1.01E-16	60.73	3,688
125	398	3.78E-17	42.09	1,771

Table 11. Final accepted values for low-temperature constants in the process model after including data from 105 °C.

Parameter	Accepted value
H_i	15 VH
H_q	77.9 VH
Q_a low temperature	153,000 J/mol
T_s low temperature	131 °C
Q_s low temperature	54,627 J/mol
$(S_0)^2_{max}$ low temperature	7,606 HV^2
P_p low temperature	6.94×10^{-17}
k low temperature	0.47

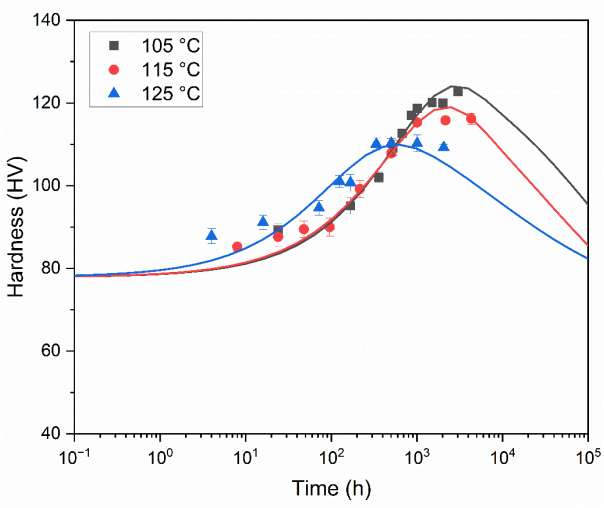

Figure 15. The optimized fit of hardness vs. aging time for the low-temperature regime after including data for 105 °C.

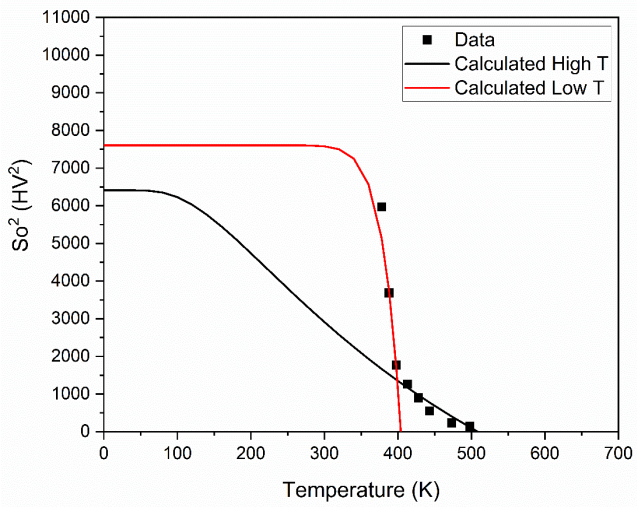

Figure 16. The plot of $(S_0)^2$ vs. aging temperature after including data for 105 °C for the low- (red line) and high-temperature regime (black line).

4. Discussion

4.1 Contribution of Strengthening Components to Hardenability

With the final parameters of the process model established, several interesting analyses and thought experiments can be performed. The contributions or solid-solution strengthening and precipitate strengthening at each temperature can be plotted and compared for their relative contributions to total hardness. A plot of the solid-solution strengthening contribution and precipitation hardening as a function of time is shown in Figure 17. Figure 17a shows that the contribution of Mg, Zn, Cu, and any other elements to solid-solution strengthening is strong, contributing approximately 63 HV in the as-quenched condition. This is mostly due to the high concertation of Mg relative to Cu and Zn. The high-temperature regime displays a modest decrease in the solid-solution strengthening contribution with time to the overaged HV with 140 °C retaining approximately 88% of the as-quenched hardness after reaching the equilibrium phase fraction of the high-temperature precipitate. Meanwhile, the decrease in hardness in the low-temperature regime is much more pronounced with 105 °C retaining 68% of the maximum solid-solution strengthening hardness. This implies that the contribution of precipitates to the overall hardness is strong in the low-temperature regime, which is reflected in Figure 17b at 105 °C. At peak hardness for 105 °C, solid-solution strengthening contributes 34% of the total hardening compared with 66% for precipitates. In contrast, solid-solution strengthening contributes 54% of the total hardening compared with 46% for precipitates at 140 °C, which demonstrates improved balance in the strengthening mechanisms.

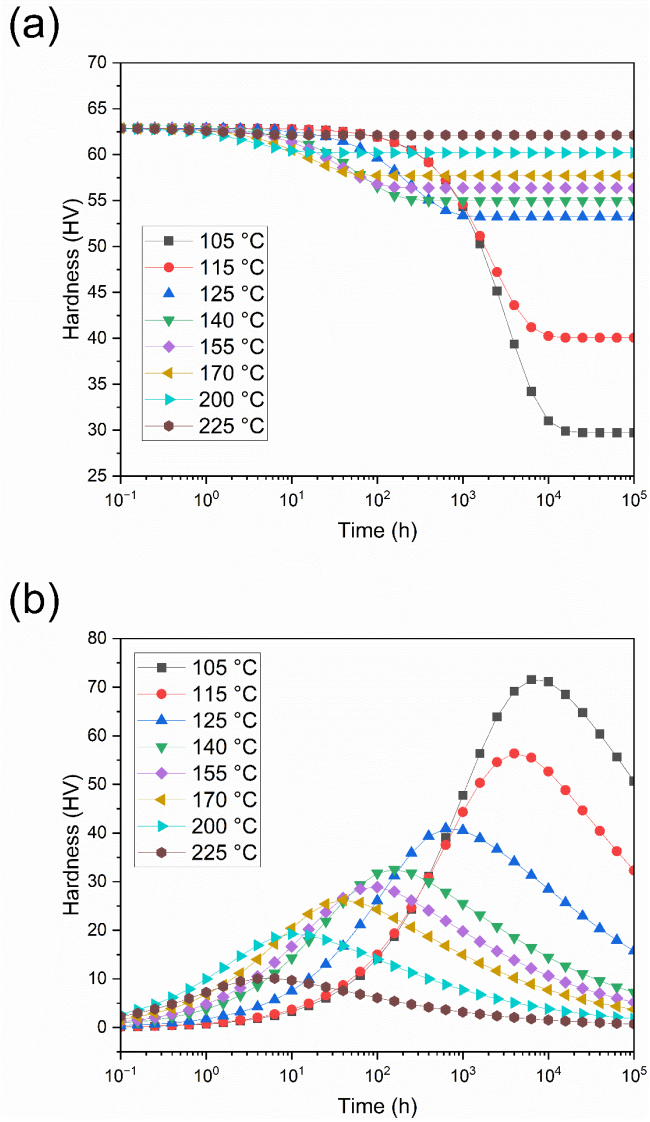

Figure 17. (a) The change in solid-solution strengthening contribution to hardness with time for each aging temperature and (b) the hardness contribution with time for strengthening precipitates.

A semilogarithmic temperature–time–hardness (T-t-H) map for the total hardness is shown in Figure 18. This surface plot predicts that a maximum hardness of 137 HV for 5180 is reached after approximately 30 years of aging at 70 °C. Further overaging at 70 °C is very slow—a 5% decrease in hardness is predicted to occur over the next 30 years. This demonstrates the excellent thermal stability of 5180 compared with the non-precipitation hardenable 5xxx series alloys such as 5083, which can experience a >5% decrease in yield strength in as few as 28 days aging at 70 °C in the H116 naval temper and after 7 days for the H131 armor temper.[14] Such mechanical degradation is linked to the precipitation and growth of the β-Al_3Mg_2 phase, which not only decreases mechanical properties but also increases

susceptibility to intergranular corrosion attack, where the β-phase along grain boundaries acts as strong local anodes to the α-matrix and increases susceptibility to various forms of environmentally assisted cracking.[15–18] This phenomenon, which is commonly referred to as sensitization, has plagued naval assets with detrimental cracking and costly repairs.[19] However, the above comparison of 5180 aged at 70 °C to 5083 is not direct because 5180 produced by conventional manufacturing will already be in the peak-aged condition that is not produced at 70 °C and 5083 contains cold work that can influence precipitation kinetics of the β-phase. The peak-aged 5180 will be manufactured at higher temperatures due to the slow-aging kinetics, which may cause a hardness increase at sensitization temperatures below 100 °C as a greater volume fraction of metastable-strengthening precipitates become thermodynamically available. At a minimum, the mechanical properties would not be expected to change for years or decades at typical sensitization temperatures of concern. This type of change can be predicted using the framework of the process model with an additional time-dependent calibration constant, which has been shown for thermal cycling and weld simulations.[6]

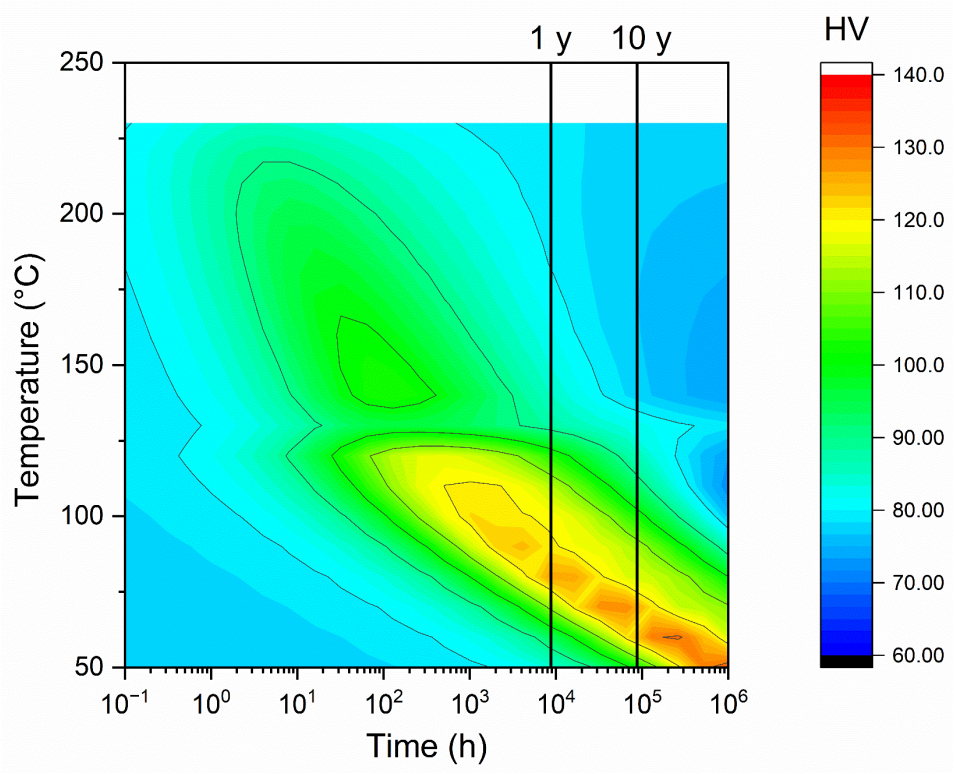

Figure 18. The T-t-H surface plot of total hardness for the optimized process model. Vertical lines indicating 1 and 10 years of aging are given.

A T-t-H map for the contribution of solid-solution strengthening and precipitate strengthening to the total hardness (as a percentage) is shown in Figure 19. This is

a useful figure for designing heat treatment with the desired material properties when used in coalition with the T-t-H map in Figure 18 to determine what the end application may be. For example, it may be more useful to have an underaged alloy in which the total strength is dominated more by the solid-solution strengthening component and the equilibrium volume fraction of precipitates has not been achieved. Furthermore, a certain type of precipitate could be favored based on aging temperature if it is deemed more beneficial to selected material properties. In general cases of an underaged alloy, the precipitates have a lower number density and are generally smaller than those in the peak-aged condition. This would benefit the corrosion behavior because detrimental pitting corrosion, stimulated by precipitate formation, will be less prevalent and uniform corrosion attack may occur, which reduces the likelihood of producing stress concentrators on the exposed surface. An underaged alloy also implies the α-face-centered cubic (FCC) matrix phase is still enriched with alloying elements compared with after the equilibrium volume fraction of precipitates is formed, which can further benefit the corrosion behavior depending on which elements are in solid solution and which elements are forming the precipitates. If more electrochemically active elements partition to the precipitates, the driving force for micro-galvanic corrosion will increase as the precipitates become more anodic to the surrounding matrix. If more noble elements partition to the precipitates, the driving force for micro-galvanic corrosion will increase but with the α-FCC matrix being preferentially attacked. In such cases, the effect of micro-galvanic corrosion should be minimized to improve overall corrosion resistance.

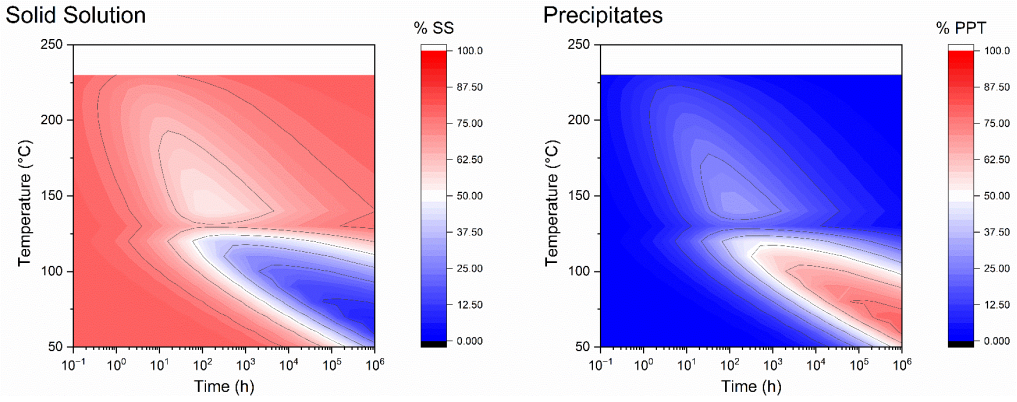

Figure 19. The T-t-H surface plots of solid-solution and precipitate strengthening (as a percentage) to total hardness for the optimized process model of 5180.

If one considers an overaged alloy with an equivalent contribution of solid-solution strengthening, the volume fraction of precipitate will be greater than in the underaged and peak-aged states because the precipitate has reached the maximum volume fraction possible, but the number density of precipitates will be less than

that of peak age, which may favor increases in ductility as dislocation movement by Orowan looping becomes more facile. However, the corrosion attack mode may switch to the detrimental intergranular attack noted with traditional 5XXX series alloys as the anodic τ-phase precipitates grow along grain boundaries and act as local galvanic cells and lead to selective dissolution of τ-phase to create stress concentrators. Like pitting corrosion, this effect needs to be minimized, but the advantage of an overaged alloy is its microstructural stability (as discussed above). Thus, balancing the electrochemical properties of the α-FCC matrix phase and precipitates through heat treatment becomes an important challenge.

The standard oxidation-reduction potential (E^o) for the primary alloying elements in 5180 is given in Table 12 where Cu is the most noble (positive) element and Mg is the most active (negative) element. The equilibrium τ-phase has a chemical structure of $Mg_{32}(Al, Zn, Cu)_{49}$ where Al, Zn, and Cu have substitutional occupancy in the lattice. Note that the metastable variants of τ-phase, which provide the precipitate strengthening, do not have the same chemical composition as equilibrium τ-phase; however, they have proximate compositions that may be more concentrated in the solute elements Mg, Cu, and Zn. The equilibrium τ-phase is composed of approximately 40 at% Mg, which signifies that the contribution of Mg to the electrochemical potential will be strong, especially given that it is 0.71 V more active than Al. In contrast, Cu has a sizeable difference in electrochemical potential compared with Al because it is approximately 2 V more noble, which indicates that the amount of Cu in the alloy is important because small amounts may make large contributions to the electrochemical potential. Finally, Zn has a standard oxidation-reduction potential 0.9 V more noble than Al, which indicates that it may modify the electrochemical potential similarly to Mg except in the positive direction.

However, the corrosion potential is kinetic and governed by the voltage–current relationship of the alloy with the oxidation and reduction reactions occurring on the alloy surface. Predicting kinetic behavior as a function of alloying content is nontrivial and experimental data is useful. To illustrate this point, recent research by the U.S. Army Combat Capabilities Development Command Army Research Laboratory has shown more than a 100-mV increase in the open-circuit potential of crossover alloys with a 0.2 at% (≈0.45 wt%) increase in Cu concentration, whereas a 2 at% (≈2 wt%) increase in the Mg concentration led to only a 25-mV decrease in the corrosion potential when accompanied by a 0.5 at% (≈1.2 wt%) at an equivalent Cu concentration.[20] This suggests that Cu is a strong electrochemical tuning knob for crossover alloys because the corrosion potential of Cu-free, equilibrium $Mg_{32}Al_{49}$ τ-phase has been measured at approximately 200 mV more anodic than 99.9999% pure Al.[21]

Table 12. The standard oxidation-reduction potentials of the main alloying elements of 5180.[22]

Reaction	E^o (V vs. SHE)	Δ vs. Al (V vs. SHE)
$Cu^{2+} + 2e^- \rightarrow Cu$	+0.342	+2.004
$Zn^{2+} + 2e^- \rightarrow Zn$	−0.762	+0.9
$Al^{3+} + 3\ e^- \rightarrow Al$	−1.662	. . .
$Mg^{2+} + 2e^- \rightarrow Mg$	−2.372	−0.71

4.2 Validity of the Process Model

The previous discussion has illustrated the usefulness of process maps that can be generated from the Shercliff and Ashby[5,6] process model. However, there are several components to the model that need to be discussed further. The process model is only as good as the data that is used to calibrate the model, and only one heat treatment of 5180 was used. Additional testing to provide a statistically validated dataset would bring more confidence in the process model fit and may improve fitting of the data. A major issue with crossover alloys is the slow precipitation kinetics that possesses a paucity of low-temperature data relevant to making predictions to sensitization at temperatures below 100 °C. Values that are forecast by the process model in the temperature regime below 100 °C relies on the assumption that there are no other strengthening phenomena that may be dominant and the current calibration of the low-temperature precipitate is valid. Iterations of the low-temperature regime have already shown how different the final calibrated values can change when iterated with (Table 11) and without (Table 9) the hardness data at 105 °C. The greatest differences occurred when comparing the volume activation energy for diffusion (Q_a), enthalpy of solution (Q_s), and the peak corrected time value P_p, which is dependent on Q_a via Equation 8. These properties are discussed in further detail (see paragraph below) regarding their importance to fitting the hardness data and tradeoff with other fitting parameters.

The value for Q_a was primarily determined by the Arrhenius relationship between aging temperature and time-to-peak hardness. The final values used in the calibration procedure were intentionally kept near to the fit value of the slope to remain physically justified. However, fitting of the hardness curves can be improved by allowing this value to vary freely during fitting. Decreases to the value of Q_a led to flattening of the predicted hardness curves, which improved fitting of overaged data because it did not show a symmetric response to hardness data at times before peak hardness. However, the optimized value of Q_a was approximately 120,000 J/mol lower than the value determined from Arrhenius fitting and deemed not valid. Comparison of the final Q_a determined for 5180 (153 kJ/mol) in the low-temperature regime shows that it is approximately 30 kJ/mol higher than the

accepted values for binary solutions of Mg and Zn in FCC-Al (Table 13), but it is within the range of typical values for solute in FCC-Al. A comparison with Q_a derived for Al–Cu and Al–Mg–Si alloys using process models (Table 14) reveals a similar discrepancy that suggests potential complex diffusion interaction within FCC-Al matrix. However, the change in slope at higher-aging temperatures suggests deviation in the mechanism governing precipitation that may be due to competitive formation and dissolution of metastable-strengthening precipitates.[23]

Table 13. The activation energy for volume diffusion (Q_a) of relevant elements in FCC-Al.

Element	Q_a (kJ/mol)	Reference
Cu	133.9	[24]
Si	117.6	[24]
Mn	211.5	[24]
Mg	120.5	[24]
Zn	116.1	[24]

Table 14. The activation energy for volume diffusion (Q_a) determined in various alloy systems using process models.

Alloy	Alloy type	Q_a (kJ/mol)	Reference
Al-2.0Cu	Al-Cu	128	[5]
Al-3.0Cu	Al-Cu	128	[5]
Al-3.5Cu	Al-Cu	128	[5]
Al-4.0Cu	Al-Cu	128	[5]
Al-4.5Cu	Al-Cu	128	[5]
6061	Al-Mg-Si	145	[5]
6082	Al-Mg-Si	130	[5]
6063	Al-Mg-Si	124.6 low	[23]
6063	Al-Mg-Si	62 high	[23]

Like Q_a, decreases in Q_s can lead to the flattening of the total aging curve to better fit the measured data. Decreases in Q_s require an increase in $(S_0)^2_{max}$ to fit the data (as related by Equation 9). However, unconstrained optimization of these two parameters for the high-temperature regime resulted in values of Q_s on the order of 10–300 J with values of $(S_0)^2_{max}$ in the hundreds of thousands (i.e., $(S_0)_{max} \approx$ 300–700 HV), which is extremely unrealistic for an aluminum alloy. Generally accepted values of Q_s from the COST 507 database for individual elements in FCC-Al (given in Table 15) show that the expected value for 5180 would be similar to that of Mg and Zn, ranging from 1 to 10 kJ/mol. However, comparison of the values in Table 15 to derived values from the process model in Table 16 show a deviation that has not been explained in other works.[5,25] In contrast to Q_s, determination of the solvus temperature from the plot of $(S_0)^2$ versus aging temperature is more robust because variation of the temperature was more limited in the iterative-fitting procedure. Other studies on 6XXX series alloys have shown good agreement for the solvus

temperatures derived from the process model to transformation temperatures detected using differential scanning calorimetry.[25] Phase transformations detected on similar 5/7-crossover alloys have shown endothermic reactions occurring in the ranges of 110–130, 180–220, and 240–250 °C, indicating ranges of potential solvus temperatures.[26] Based on these endotherms and exothermic reaction in other studies,[27,28] age hardening in the low-temperature regime is attributed to "*GPII/τ*" precipitates, which are sphere-like, whereas the high-temperature regime is likely "*τ*" precipitates, which are lathe- or rod-like. As such, other process or strength models need to be explored to confirm or invalidate the predictions made in this work. It is hypothesized that the process model can be improved when considering the shape of precipitates, which were assumed as spherical for this process model. Further improvements can be made when not assuming the age-hardening response is symmetrically distributed, by considering the fraction and interparticle spacing of precipitates and grain-boundary strengthening. Finally, the simultaneous contribution of multiple precipitates to the mechanical response needs to be considered, which will likely improve fitting near the transition temperature.

Table 15. The solution-free energy (Q_s) of relevant elements in FCC-Al.

Element	Q_s (kJ/mol)	Reference
Cu	–53.52	[29]
Si	–3.144	[29]
Mn	–69.3	[29]
Mg	4.971	[29]
Zn	7.297	[29]

Table 16. The solution-free energy (Q_s) determined in various alloy systems using process models.

Alloy	Alloy type	Q_s (kJ/mol)	Reference
Al-2.0Cu	Al-Cu	25	[5]
Al-3.0Cu	Al-Cu	25	[5]
Al-3.5Cu	Al-Cu	25	[5]
Al-4.0Cu	Al-Cu	25	[5]
Al-4.5Cu	Al-Cu	25	[5]
6061	Al-Mg-Si	30	[5]
6082	Al-Mg-Si	30	[5]

5. Conclusions

This report documents the first reported process model of crossover 5xxx series aluminum alloy 5180. The following can be concluded:

- The process model proposed by Shercliff and Ashby[5,6] provided a good fit to the experimental data with a high- and low-temperature strengthening precipitate, suggesting that two metastable precipitates are responsible for the precipitation-hardening response.
- Fitting the hardening response of the low-temperature precipitate was difficult due to lack of a defined time-to-peak age, which decreases confidence in the fit and projection of data below 115 °C.
- An examination of the solid-solution and precipitate strengthening components as a function of time and temperature has provided new insights to optimize the heat treatment of 5180.
- A prediction of the change in hardness at temperatures below 100 °C revealed greatly improved thermal stability compared with conventional 5XXX series alloys such as 5083, assuming that low-temperature fitting with the process model is valid.

6. References

1. Lin J, inventor; ALCOA Inc, assignee. Heat treatable aluminum alloys having magnesium and zinc and methods for producing the same. United States patent US9315855b2. 2016 Apr 19.

2. Stemper L, Tunes MA, Tosone R, Uggowitzer PJ, Pogatscher S. On the potential of aluminum crossover alloys. Prog Mater Sci. 2022;124:100873. https://doi.org/10.1016/j.pmatsci.2021.100873

3. Hou S, Liu P, Zhang D, Zhang J, Zhuang L. Precipitation hardening behavior and microstructure evolution of Al–5.1 Mg–0.15Cu alloy with 3.0Zn (wt%) addition. J Mater Sci. 2018;53(5):3846–3861. https://doi.org/10.1007/s10853-017-1811-1

4. Stemper L et al. Giant hardening response in AlMgZn(Cu) alloys. Acta Mater. 2021;206:116617. https://doi.org/10.1016/j.actamat.2020.116617

5. Shercliff HR, Ashby MF. A process model for age hardening of aluminium alloys—I. The model. Acta Metall Mater. 1990;38(10):1789–1802. https://doi.org/10.1016/0956-7151(90)90291-n

6. Shercliff HR, Ashby MF. A process model for age hardening of aluminium alloys—II. Applications of the model. Acta Metall Mater. 1990;38(10):1803–1812. https://doi.org/10.1016/0956-7151(90)90292-O

7. Deschamps A, Brechet Y. Influence of predeformation and aging of an Al–Zn–Mg alloy—II. Modeling of precipitation kinetics and yield stress. Acta Mater. 1998;47(1):293–305. https://doi.org/10.1016/S1359-6454(98)00296-1

8. Deschamps A, Livet F, Bréchet Y. Influence of predeformation on aging in an al–zn–mg alloy—I. Microstructure evolution and mechanical properties. Acta Mater. 1998;47(1):281–292. https://doi.org/10.1016/S1359-6454(98)00293-6

9. Zhu AW, Csontos A, Starke EA. Computer experiment on superposition of strengthening effects of different particles. Acta Mater. 1999;47(6):1713–1721. https://doi.org/10.1016/S1359-6454(99)00077-4

10. Zhu AW, Starke EA. Strengthening effect of unshearable particles of finite size: a computer experimental study. Acta Mater. 1999;47(11):3263–3269. https://doi.org/10.1016/S1359-6454(99)00179-2

11. Myhr OR, Grong Ø, Andersen SJ. Modelling of the age hardening behaviour of Al–Mg–Si alloys. Acta Mater. 2001;49(1):65–75. https://doi.org/10.1016/S1359-6454(00)00301-3

12. Robson JD. Microstructural evolution in aluminium alloy 7050 during processing. Mater Sci Eng A. 2004;382(1):112–121. https://doi.org/10.1016/j.msea.2004.05.006

13. ASTM E140-12B(2019)E1. Standard hardness conversion tables for metals relationship among Brinell hardness, Vickers hardness, Rockwell hardness, superficial hardness, Knoop hardness, scleroscope hardness, and Leeb hardness. ASTM International; 2019.

14. Murdoch H, Magagnosc D, Blohm L, Yin D, Walter T. An analysis of variability in sensitization behavior of 5083-h131 and the impacts on yield strength. DEVCOM Army Research Laboratory (US): 2023. Report No.: ARL-TR-9718.

15. Crane CB, Kelly RG, Gangloff RP. Crack chemistry control of intergranular stress corrosion cracking in sensitized Al-Mg. Corrosion. 2015;72(2):242–263. https://doi.org/10.5006/1852

16. Golumbfskie WJ et al. Survey of detection, mitigation, and repair technologies to address problems caused by sensitization of Al-Mg alloys on Navy ships. Corrosion. 2015;72(2):314–328. https://doi.org/10.5006/1916

17. Henry Holroyd NJ, Scamans GM. Environmental degradation of marine aluminum alloys—past, present, and future. Corrosion. 2015;72(2):136–143. https://doi.org/10.5006/1927

18. Lim MLC, Kelly RG, Scully JR. Overview of intergranular corrosion mechanisms, phenomenological observations, and modeling of aa5083. Corrosion. 2015;72(2):198–220. https://doi.org/10.5006/1818

19. Navy ship modernization: poor cruiser outcomes demonstrate need for better planning and quality oversight in future efforts. Government Accountability Office (US); 2024. Report No.: GAO-25-106749.

20. Cain TW, Blohm LM. On the corrosion behavior of precipitation hardenable 5xxx series aluminum alloys. DEVCOM Army Research Laboratory (US). 2025. Report No: ARL-TR-10126.

21. Birbilis N, Buchheit RG. Electrochemical characteristics of intermetallic phases in aluminum alloys - an experimental survey and discussion. J Electrochemi Soc. 2005;152(4):B140–B151. https://doi.org/10.1149/1.1869984

22. Vanysek P. Electrochemical series. In: Handbook of chemistry and physics. CRC Press; 2013. p. 5-80–5-89.

23. Nandy S, Kumar Ray K, Das D. Process model to predict yield strength of aa6063 alloy. Mater Sci Eng A. 2015;644:413–424. https://doi.org/10.1016/j.msea.2015.07.070

24. Du Y et al. Diffusion coefficients of some solutes in FCC and liquid Al: critical evaluation and correlation. Mater Sci Eng A. 2003;363(1):140–151. https://doi.org/10.1016/S0921-5093(03)00624-5

25. Rometsch PA, Schaffer GB. An age hardening model for Al–7Si–Mg casting alloys. Mater Sci Eng A. 2002;325(1):424–434. https://doi.org/10.1016/S0921-5093(01)01479-4

26. Tang HP et al. Effects of aging treatment on the precipitation behaviors and mechanical properties of Al-5.0Mg-3.0Zn-1.0Cu cast alloys. J Alloys Compd. 2020;842:155707. https://doi.org/10.1016/j.jallcom.2020.155707

27 Hou SL, Zhang D, Ding QW, Zhang JS, Zhuang LZ. Solute clustering and precipitation of Al-5.1Mg-0.15Cu-xZn alloy. Mat Sci Eng A-Struct. 2019;759:465–478. https://doi.org/10.1016/j.msea.2019.05.066

28. Klein T et al. Wire-arc additive manufacturing of a novel high-performance Al-Zn-Mg-Cu alloy: processing, characterization and feasibility demonstration. Addit Manuf. 2021;37:101663. https://doi.org/10.1016/j.addma.2020.101663

29. Ansara I, Dinsdale AT, Rand MH. Cost 507: thermochemical database for light metal alloys. Vol 2. Office for Official Publications of the European Communities; 1998.

List of Symbols, Abbreviations, and Acronyms

AA	Aluminum Alloy
Al	Aluminum
ASTM	American Society for Testing and Materials
Bal	Balance
CAMI	Coated Abrasive Manufacturer's Institute
Cr	Chromium
Cu	Copper
FCC	Face-Centered Cubic
Fe	Iron
GRG	Generalized Reduced Gradient
H_i	Intrinsic Hardness
ΔH_{ppt}	Change in Precipitate Hardness
HRB	Hardness Rockwell B
ΔH_{ss}	Change in Solid-Solution Hardness
ΔH_{SS}	Final Solid-Solution Strengthening Contribution
ΔH_{ssi}	Initial Solid-Solution Strengthening Hardening Contribution after Quenching
$\Delta H_{ss,oa}$	Solid-Solution Strengthening Overaged Hardness
HV	Vickers Hardness Value
k	Solid-Solution Time Constant
kgf	Kilogram Force
Mg	Magnesium
Mn	Manganese
Ni	Nickel
P	Temperature-Corrected Time
P_p	Value of P at the Peak in the Aging Curve

Q_a	Activation Energy for Volume Diffusion of Atoms in the Matrix
Q_s	Solvus Enthalpy
R	Ideal Gas Constant
Sc	Scandium
SE	Squared Error
SHE	Standard Hydrogen Electrode
Si	Silicon
SiC	Silicon Carbide
S_o	Precipitate Strength
$(S_o)_{max}$	Strength Parameter
t	Time
T	Isothermal Aging Temperature
t_1	Constant Related to the Time-to-Peak Hardness
TEM	Transmission Electron Microscopy
Ti	Titanium
t_p	Time-to-Peak Hardness
T_s	Metastable Solvus Temperature
T-t-H	Temperature–Time–Hardness
VH	Vickers Hardness
Zn	Zinc
Zr	Zirconium

1 (PDF)	DEFENSE TECHNICAL INFORMATION CTR DTIC OCA
1 (PDF)	DEVCOM ARL FCDD RLB CB TECH LIB